PNAS RESEARCH ARTICLE | BIOPHYSICS AND COMPUTATIONAL BIOLOGY

Structural basis of higher order oligomerization of KSHV inhibitor of cGAS

Debipreeta Bhowmik[a,1], Yuan Tian[a,1], Bing Wang[a], Fanxiu Zhu[a,2], and Qian Yin[a,b,2]

Edited by Hao Wu, Harvard Medical School, Boston, MA; received January 7, 2022; accepted June 14, 2022

Kaposi's sarcoma–associated herpesvirus (KSHV) inhibitor of cyclic GMP–AMP synthase (cGAS) (KicGAS) encoded by ORF52 is a conserved major tegument protein of KSHV and the first reported viral inhibitor of cGAS. In our previous study, we found that KicGAS is highly oligomerized in solution and that oligomerization is required for its cooperative DNA binding and for inhibiting DNA-induced phase separation and activation of cGAS. However, how KicGAS oligomerizes remained unclear. Here, we present the crystal structure of KicGAS at 2.5 Å resolution, which reveals an "L"-shaped molecule with each arm of the L essentially formed by a single α helix (α1 and α2). Antiparallel dimerization of α2 helices from two KicGAS molecules leads to a unique "Z"-shaped dimer. Surprisingly, α1 is also a dimerization domain. It forms a parallel dimeric leucine zipper with the α1 from a neighboring dimer, leading to the formation of an infinite chain of KicGAS dimers. Residues involved in leucine zipper dimer formation are among the most conserved residues across ORF52 homologs of gammaherpesviruses. The self-oligomerization increases the valence and cooperativity of interaction with DNA. The resultant multivalent interaction is critical for the formation of liquid condensates with DNA and consequent sequestration of DNA from being sensed by cGAS, explaining its role in restricting cGAS activation. The structure presented here not only provides a mechanistic understanding of the function of KicGAS but also informs a molecular target for rational design of antivirals against KSHV and related viruses.

KicGAS | ORF52 | higher order oligomerization | cGAS | DNA binding

Significance

Kaposi's sarcoma–associated herpesvirus (KSHV) inhibitor of cyclic GMP–AMP synthase (cGAS) (KicGAS) is a major tegument protein of KSHV and crucial for the evasion of host immune responses. KicGAS self-assembles to function, yet the structural basis of assembly was unknown. Here, we present the crystal structure of KicGAS forming a higher order assembly. The structure reveals how oligomerization of KicGAS mediates multivalent interaction with DNA required for cGAS inhibition. Comparison with homologous protein structures reveals diverse oligomerization characteristics in addition to conserved features, highlighting divergence in virus evolution.

Cyclic GMP-AMP synthase (cGAS) is a key and ubiquitous pathogen recognition receptor that detects aberrant and mislocated DNAs arising from pathogen invasions or genotoxic stresses. cGAS is a signaling enzyme with nucleotidyltransferase activity that is activated upon binding to double-stranded DNA (1, 2). Activated cGAS catalyzes the synthesis of cyclic GMP–AMP (cGAMP) that acts as a secondary messenger to be recognized by stimulator of interferon genes (STING) in the same cell or neighboring cells and ultimately activates the TBK1–IRF3 pathway to induce the expression of type I interferons (IFNs) and other proinflammatory cytokines (3, 4). The DNA-induced enzymatic activity, cGAMP-mediated secondary messenger amplification, and IFN- and receptor-mediated signaling transduction could theoretically enable the cGAS–STING–IFN immune surveillance pathway as the first responder to not only efficiently detect abnormal pathogen-associated molecular patterns or danger/damage-associated molecular patterns but also massively amplify and spread the signaling to trigger innate immune responses and subsequently adaptive immune responses. The cGAS–STING pathway has been shown to be essential for sensing diverse groups of viruses, including viruses with large DNA genomes such as herpesviruses. Yet herpesviruses in general do not induce massive IFN response (5–7), implying efficient viral counteracting mechanisms. Indeed, since the discovery of cGAS, diverse viral evasion mechanisms have been reported, and herpesviruses were found to devote multiple gene products in antagonizing cGAS–STING DNA sensing (8, 9). Among them, Kaposi's sarcoma–associated herpesvirus (KSHV) inhibitor of cGAS (KicGAS) is the first reported viral cGAS antagonist that inhibits cGAS activity (10).

KicGAS is encoded by *ORF52* of KSHV, a human DNA tumor virus causing Kaposi's sarcoma, primary effusion lymphoma, and multicentric Castleman's disease (11–13). KicGAS is a small protein of 131 amino acids (aa). It is a positively charged and abundant virion-contained tegument protein conserved among gammaherpesviruses. Although no homolog has been identified in betaherpesviruses, ORF52 is found to be structurally related to VP22 in alphaherpesviruses such as herpes simplex virus 1 (HSV-1) (14). We have reported that KicGAS and its homologs from other gammaherpesviruses inhibit cGAS activity in vitro (15). Recently, we and others found that KicGAS undergoes liquid–liquid phase separation upon binding with DNA (15, 16).

Author affiliations: [a]Department of Biological Science, Florida State University, Tallahassee, FL 32306; and [b]Institute of Molecular Biophysics, Florida State University, Tallahassee, FL 32306

Author contributions: D.B., Y.T., F.Z., and Q.Y. designed research; D.B., Y.T., B.W., and Q.Y. performed research; D.B., Y.T., B.W., F.Z., and Q.Y. analyzed data; and D.B., Y.T., F.Z., and Q.Y. wrote the paper.

The authors declare no competing interest.

This article is a PNAS Direct Submission.

[1]D.B. and Y.T. contributed equally to this work.

[2]To whom correspondence may be addressed. Email: yin@bio.fsu.edu or fzhu@bio.fsu.edu.

This article contains supporting information online at http://www.pnas.org/lookup/suppl/doi:10.1073/pnas.2200285119/-/DCSupplemental.

Published August 8, 2022.

The DNA-induced phase separation of KicGAS correlates well with its ability to inhibit cGAS. Any mutations that abrogate DNA-induced KicGAS phase separation also abolish the inhibition of cGAS phase separation and activity. Purified KicGAS protein exists as an oligomer and binds to DNA cooperatively (15). Mutations that disrupt KicGAS oligomerization also abolish DNA binding and cGAS inhibition, suggesting KicGAS oligomerization is critical for its functions (10, 15). Collectively, oligomerization of KicGAS underlies cooperative and multivalent interaction with DNA that is essential for phase separation of KicGAS itself and the inhibition of cGAS phase separation and activity (15, 16).

Despite the critical roles of KicGAS oligomerization in DNA binding, DNA-induced phase separation, and cGAS inhibition, the structural basis of KicGAS oligomerization remained unknown. To gain structural insights of KicGAS oligomerization, we have determined the crystal structure of the core region of KicGAS (aa 9–95, henceforth named KicGAS$^{9\text{-}95}$) at 2.5 Å resolution. The structure reveals a dimeric association of KicGAS, with each monomer containing three α helices. The dimers further oligomerize through leucine zippers formed by the N-terminal α1 helices between neighboring dimers, essentially forming an infinite chain of KicGAS dimers in the crystal lattice. This structure not only confirms many of our previous observations but also enables us to understand the way oligomerization of KicGAS mediates multivalent interactions with DNA, the key feature that forms the basis for cGAS inhibition.

Results

KicGAS Forms Heterogenous Oligomers in Solution. To better understand the biochemical and structural features of KSHV KicGAS/ORF52 (KicGAS henceforth), we purified full-length recombinant KicGAS from *Escherichia coli*. We noticed that KicGAS eluted from size exclusion chromatography at a very early position (~58.6 mL on a HiLoad 16/600 column) (Fig. 1*A*), suggesting oligomeric form or elongated shape. In comparison, the tetrameric MHV-68 homolog eluted at ~69.7 mL, and the dimeric HSV-1 homolog VP22^{core} (VP22 aa 174–281) eluted at ~91.4 mL (*SI Appendix*, Fig. S1). Serial dilution from 200 to 30 μM steadily shifted KicGAS elution positions to the right, suggesting oligomerization is concentration-dependent (Fig. 1*A*). We performed sedimentation velocity analytical ultracentrifugation (SV-AUC) experiments to further characterize the hydrodynamic behavior of KicGAS. At 0.14 mg/mL (10 μM), KicGAS existed predominantly as a tetramer (Fig. 1 *B* and *C*). In addition to tetramers, two-dimensional spectral analysis (with Monte Carlo) revealed the presence of hexameric proteins in a small fraction. The frictional ratio f/f_0 is a numerical descriptor of the particle's anisotropy. While globular proteins typically have a f/f_0 value of 1.2–1.4, higher f/f_0 values indicate asymmetric or even rod-like shape of the protein (17). For the tetrameric and hexameric species, the f/f_0 values are 1.7 and 2.6 respectively, suggesting KicGAS oligomers assume an elongated shape (Fig. 1*C*).

Crystal Structure Reveals Dimer as the Repeating Unit of KicGAS. Because the solution behavior of KicGAS differs substantially from that of its homologs in MHV-68 and HSV-1, we are curious of the structure and organization of KicGAS. We carried out extensive screening to identify suitable conditions to crystallize KicGAS. Based on sequence conservation and secondary structure prediction, we generated two truncated versions of KicGAS, KicGAS$^{9\text{-}104}$ and KicGAS$^{9\text{-}95}$, by removing less conserved and disordered regions at *N*- and C-termini of full-length KicGAS (Fig. 2*A* and *SI Appendix*, Fig. S2). Both KicGAS$^{9\text{-}104}$ and KicGAS$^{9\text{-}95}$ eluted at positions consistent with oligomerization (Fig. 2*B*), indicating the predicted structured α helical regions are the major contributors to KicGAS oligomerization, and removal of the disordered regions does not alter the overall features of full-length KicGAS. Both KicGAS$^{9\text{-}104}$ and KicGAS$^{9\text{-}95}$ bound to DNA and inhibited cGAS activity, though with less efficiency (*SI Appendix*, Fig. S3). Among full-length and truncated versions of KicGAS, only KicGAS$^{9\text{-}95}$ successfully crystallized and diffracted to atomic resolution. We introduced a single mutation L62M to increase phasing power. Substituting Met for Leu62 did not alter characteristics of KicGAS$^{9\text{-}95}$ (Fig. 2*B*), so we will not specify L62M in the following description of crystal structure and discussion. We crystallized selenomethionyl KicGAS$^{9\text{-}95}$ in the space group of I222 and solved the structure by using molecular replacement coupled with single-wavelength anomalous diffraction. The KicGAS$^{9\text{-}95}$ structure was refined to 2.5 Å resolution with R_{work}/R_{free} = 0.2246/0.2655 (*SI Appendix*, Table S1).

There are two KicGAS$^{9\text{-}95}$ molecules in one asymmetric unit, forming a dimer. Each molecule is composed of three α helices (Fig. 2*C*). While α3 folds back onto α2, α1 swings out almost orthogonal to the α2–α3 plane. Overall, the molecule assumes an "L" shape with α1 forming the short edge of the "L" shape and α2 forming the longer edge. The intramolecular

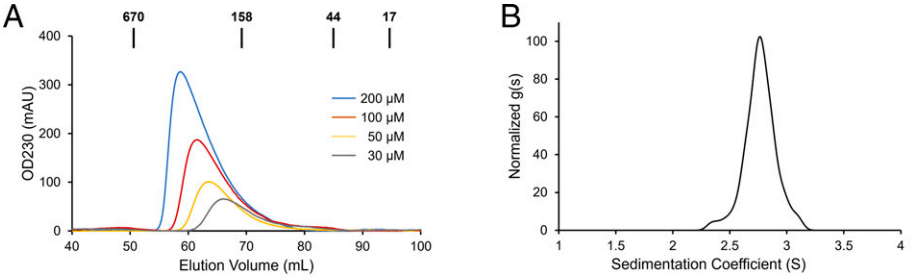

C

	Molecular Weight (Da)	Oligomeric Status	Sedimentation coefficient	Frictional ratio (f/f0)	Percentage
Comp 1	48,950	tetramer	2.7642e-13	1.70	66.7 %
Comp 2	77,098	hexamer	2.4512e-13	2.60	10.1 %
Comp 3	31,829	dimer	3.4259e-13	1.03	8.2 %

Fig. 1. KicGAS forms oligomers in solution. (*A*) KicGAS forms concentration-dependent oligomers as characterized by size exclusion chromatography; Molecular standards are marked on the profile. OD230, optical density at 230 nm. (*B*) Histogram envelope plot showing the sedimentation coefficient distribution from the SV-AUC experiment with KicGAS. (*C*) Hydrodynamic properties of major KicGAS species in solution as determined in (*B*).

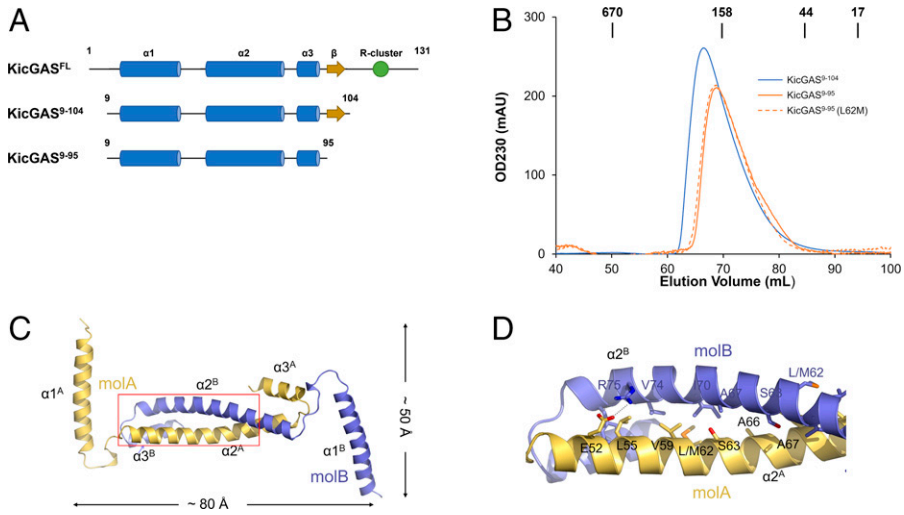

Fig. 2. KicGAS repeating unit is a dimer. (*A*) Diagrams of full-length and truncated versions of KicGAS. (*B*) Size exclusion chromatography profiles of KicGAS$^{9\text{-}104}$, KicGAS$^{9\text{-}95}$, and KicGAS$^{9\text{-}95}$ (L62M). OD230, optical density at 230 nm. (*C*) Dimer structure of KicGAS$^{9\text{-}95}$ with one chain (molA) colored in yellow and the other (molB) in blue. The secondary structure elements are labeled with chain ID as superscript. (*D*) Close-up view of the dimer interface mediated by α2 helix (red rectangle in (*C*)). Since the interface is symmetrical, only the left half is shown.

interface between α2 and α3 is hydrophobic, with contributions from I77 and F78 on α2 and V87, A90, L91, and L94 on α3 (*SI Appendix*, Fig. S4). The two molecules superpose well with each other, with an rmsd of 2.787 Å across 81 Cαs. The individual regions superpose even better. The α2–α3 regions superpose with an rmsd of 0.429 Å across 45 Cαs, and the two α1 helices superpose with an rmsd of 0.421 Å across 23 Cαs. The major difference between the two copies of KicGAS$^{9\text{-}95}$ is the angles formed between the α1 and α2–α3 planes. In molecule A the angle is about 87°; in molecule B, α1 swings slightly outwards, forming an angle of 93° (*SI Appendix*, Fig. S5*A*).

The two molecules of KicGAS form a "Z"-shaped stable dimer with pseudo-twofold symmetry. The dimer interface is mediated mostly by α2 with additional contributions from α3. The two α2 helices intertwined in an antiparallel and symmetrical fashion, burying a total area of 2,864 Å^2. The complex formation significance score (a parameter indicating the significance of an interface for assembly formation, https://www.ebi.ac.uk/msd-srv/prot_int/pi_ilist_css.html) is 1.000, indicating the interface plays an essential role in dimer formation. The interactions are mostly hydrophobic, contributed by sidechains of multiple aliphatic residues across the α2 helix. However, at either end of the dimer, a pair of charged residues, E52 and R75, seal the dimer by forming strong salt bridges (Fig. 2*D*). A secondary dimer interface is between the α1–α2 linker and the N terminus of α2 in one molecule and the α2–α3 linker in the other molecule (*SI Appendix*, Fig. S5*B*). P45 and L46 in one molecule and V82 and T83 in the other molecule form the hydrophobic core of this interface. The NH group of L46 forms a hydrogen bond with the carbonyl oxygen of V82 of the other molecule. Additional asymmetrical interactions contribute to the dimer interfaces. D43 and Q54 in molecule B form hydrogen bonds/salt bridges with K85 and Q84 in molecule A, respectively (*SI Appendix*, Fig. S5*B*).

Polymerization of KicGAS Dimers in Crystal and Solution. The most interesting feature of the KicGAS structure is that the α1 helix in molecule A (molA) forms a leucine zipper with the α1 helix in a symmetry-related molecule B (molB′), essentially forming an infinite chain of KicGAS dimers in the crystal lattice (Fig. 3*A*). Together, the two α1 helices bury an area of 1,417 Å^2. The completely (L24, E27, N28, L31) or highly conserved residues (L17, I21, R32, and L35) all participate in leucine zipper formation (Fig. 3*B* and *SI Appendix*, Fig. S2). While the leucines and the isoleucine form the hydrophobic core of the α1 dimer, E27, N28, and R32 reinforce the dimer by forming salt bridges and hydrogen bonds with charged and polar residues on the other α1 helix (Fig. 3*B*). Previously, we have shown that single mutation of I21, L24, N28, or L31 to alanine shifted KicGAS elution positions from oligomers to dimers (15). Here we found that change of L17 to the bulky arginine residue also shifted the peak elution position from oligomers to dimers, affirming the critical roles of these residues in forming α1-mediated dimer interface (*SI Appendix*, Fig. S6*A*). Mutating L35 to alanine or arginine also shifted the elution positions to the right, but the effect was less prominent compared to L17R (*SI Appendix*, Fig. S6*A*). Consistent with disruption in oligomerization, all three mutants exhibited reduced DNA binding, DNA-induced phase separation, and suppression of cGAS activity (*SI Appendix*, Fig. S6 *B*–*E*).

We then used electron microscopy to examine whether the polymeric structure observed in crystal is also present in solution. Negative stain electron microscopy of purified KicGAS$^{9\text{-}95}$ revealed thin filaments of various lengths (Fig. 3*C*). The lengths of the filaments are a few hundred nanometers, corresponding to at least 25 KicGAS$^{9\text{-}95}$ dimers in most of the filaments. The diameter of the thin filaments is about 6 nm, close to the width (~5 nm) of a single KicGAS$^{9\text{-}95}$ dimer (Figs. 2*A* and 3*C*). This result suggested that KicGAS dimers are organized along a single axis, resulting in long filaments. In contrast, we observed only small particles and no filaments with the oligomerization deficient mutant protein L17R, suggesting α1-mediated oligomerization is required for KicGAS polymer formation (*SI Appendix*, Fig. S6).

MHV-68 ORF52 shares 32% sequence identity and 65% similarity to KSHV KicGAS, and its monomer structure shares the same α1–α2–α3 secondary structure arrangement (*SI Appendix*, Fig. S2) (18). In solution and crystal, MHV-68 ORF52 forms a tetramer through dimerization of two dimers. Two molecules of MHV-68 ORF52 form a dimer via the same α2–α3 interface as in KicGAS (Fig. 3*D*). The two α1 helices in the dimer further form two leucine zippers with the two α1 helices of an opposing dimer, completing the closed tetramer (Fig. 3*D*). The α2–α3 frameworks of KSHV and MHV-68 ORF52s aligned very well

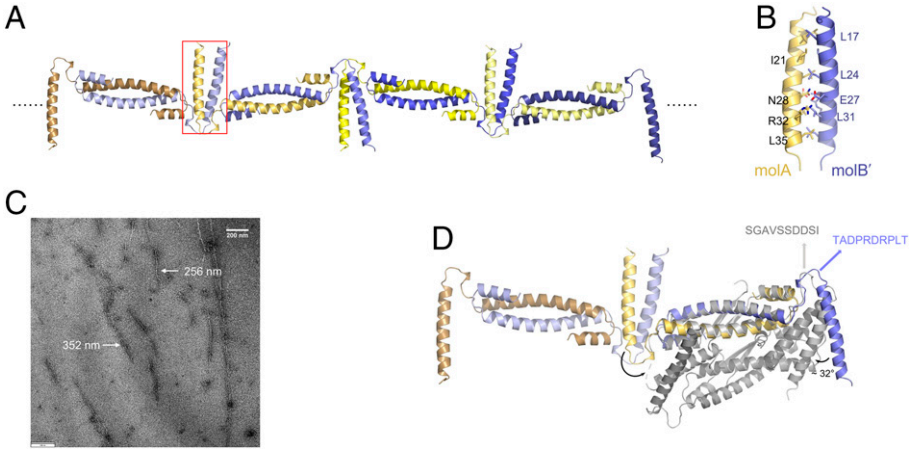

Fig. 3. KicGAS dimer further polymerizes via α1 leucine zipper. (*A*) KicGAS forms α1-mediated infinite chain of dimers in the crystal lattice. Molecules A and B in each dimer are colored in different shades of yellow and blue, respectively. (*B*) Highly conserved hydrophobic residues mediate leucine zipper formation between α1 helices of molecule A (molA) in one dimer and molecule B (molB′) in a symmetry-related dimer. (*C*) Negative stain electron microscopy showing KicGAS$^{9\text{-}95}$ filaments. KicGAS$^{9\text{-}95}$ concentration: 3.4 mg/mL Scale bar: 200 nm. (*D*) Superposition of KSHV KicGAS tetramer (yellow and blue) with MHV-68 ORF52 tetramer (gray, PDB ID: 2OA5). Black arrows mark the movement of the two α1 helices in the structures. The sequences of the α1–α2 loops are labeled next to the loops.

with each other, with an rmsd of 0.900 Å across 40 Cαs in the α2–α3 region (Fig. 3*D*). The α1 leucine zippers in the two structures are almost identical, with an rmsd of 0.234 Å across 19 Cαs (*SI Appendix*, Fig. S7).

A striking difference is the orientations of α1 helices relative to the α2–α3 framework. In KicGAS, the two α1 helices assume similar orientations, both orthogonal to the α2–α3 framework. In the MHV-68 ORF52 structure, however, one α1 helix bends ~32° toward the α2–α3 framework, while the other α1 helix swings more than 270°, contacting the other side of the α2–α3 framework (Fig. 3*D*). Indeed, in the latter large-scale movement, the linker connecting α1 and α2 in that MHV-68 molecule is invisible in electron density, further highlighting the flexible nature of this linker.

The more rigid nature of KicGAS structure probably arises partially from the two prolines, P41 and P45, in the α1–α2 linker (Figs. 3*D* and 4*A* and *SI Appendix*, Fig. S8). The two prolines are conserved mostly in gammaherpesviruses of primates but not in ORF52 of murine MHV-68 (Fig. 4*A* and *SI Appendix*, Fig. S8). When we changed the two prolines to serine and isoleucine, their counterparts in MHV-68 ORF52, oligomerization of the P41S/P45I mutant protein decreased (Fig. 4*B*).

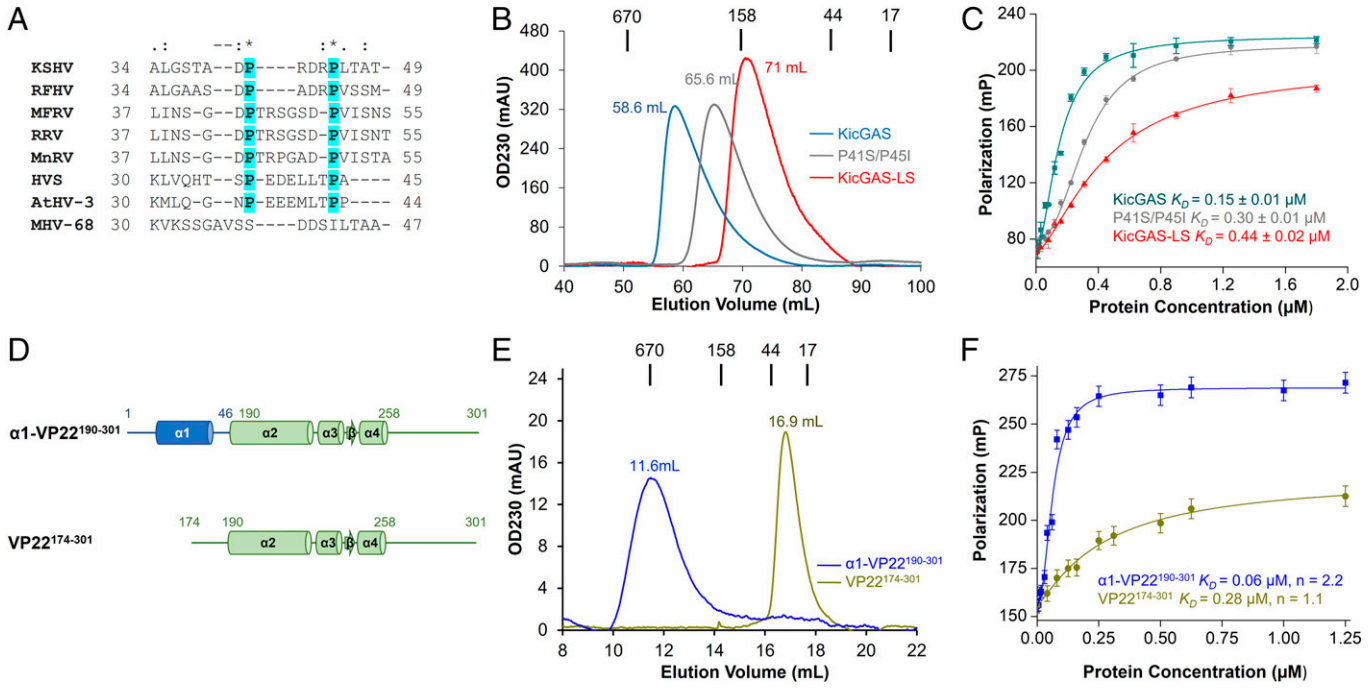

Fig. 4. Unique α1–α2 linker sequence dictates KicGAS oligomerization. (*A*) Alignment of the linker sequences of KicGAS homologs from gamma-2 herpesviruses. The two conserved proline residues are highlighted in cyan. RFHV, Retroperitoneal fibromatosis herpesvirus; RRV, Rhesus monkey rhadinovirus; MFRV, Macaca fuscata rhadinovirus; MnRV, Macaca nemestrina rhadinovirus 2; HVS, Herpesvirus saimiri; AtHV-3, Ateline herpesvirus 3; MHV-68, Murid herpesvirus 68. (*B*) Size exclusion chromatography profiles of KicGAS, the P41S/P45I mutant, and the linker switch KicGAS-LS mutant. OD230, optical density at 230 nm. (*C*) Fluorescence polarization binding curves of KicGAS, P41S/P45I, and KicGAS-LS with ISD45. (*D*) Schematic of the fusion of the N-terminal α helix of KicGAS to the VP22 core domain (α1-VP22$^{190\text{-}301}$). (*E*) Size exclusion chromatography profiles of α1-VP22$^{190\text{-}301}$ and VP22$^{174\text{-}301}$. (*F*) Fluorescence polarization binding curves of α1-VP22$^{190\text{-}301}$ and VP22$^{174\text{-}301}$ with ISD45.

Other intramolecular interactions contribute to hold the α1 helix in orthogonal position in KicGAS structure. In molecule B, R44 in the α1–α2 linker and E50 in α2 form a salt bridge, stabilizing the conformation. In molecule A, R44 swings toward the base of α1, breaking the salt bridge with E50 and forming two hydrogen bonds with carbonyl oxygens of G36 and T38 instead (*SI Appendix*, Fig. S9). The difference in R44 sidechain conformations probably contributes to the slight difference in α1 orientation of KicGAS as well. Replacement of KicGAS α1–α2 linker with MHV-68 sequence (KicGAS-LS) dramatically reduced the level of KicGAS oligomerization to the level of that of MHV-68 ORF52 (Fig. 4*B* and *SI Appendix*, Fig. S1), confirming the α1–α2 linker indeed controls the orientation of α1 helix and consequently affects the oligomerization status of the molecules. As compared to the wild type KicGAS, P41S/P45I and KicGAS-LS mutations resulted in twofold and threefold reduction in DNA binding, respectively (Fig. 4*C*). Upon binding to DNA, KicGAS further oligomerizes and forms higher order structures, probably in the form of liquid condensates (*SI Appendix*, Fig. S10*A*) (15). These linker mutants exhibited reduced propensity to undergo DNA-induced phase separation, as shown by reduced turbidity formation (*SI Appendix*, Fig. S10*B*). Consequently, their abilities to inhibit cGAS were also diminished (*SI Appendix*, Fig. S10 *C* and *D*).

KicGAS was considered unique to gammaherpesviruses because no alphaherpesviral or betaherpesviral protein bears sufficient sequence similarity to KicGAS. However, the structure of the core region of VP22 (aa 174–281) of HSV-1, an alphaherpesvirus, displays striking similarity to MHV-68 ORF52 and marks it as a structural homolog of KicGAS and MHV-68 ORF52 (14). $VP22^{174\text{-}281}$ exists exclusively as a dimer in solution, where the interface is formed by a pair of α helices equivalent to α2 and α3 in KicGAS and MHV-68 ORF52 (*SI Appendix*, Fig. S11) (14). HSV-1 $VP22^{174\text{-}281}$ structure superposes with KicGAS structure, with an rmsd of 4.2 Å across 30 Cαs (*SI Appendix*, Fig. S11). Without a region equivalent to the α1 helix, the VP22 core does not further tetramerize or oligomerize. However, when we fused the first 46 aa of KicGAS that contains α1 helix and α1–α2 linker to the N terminus of $VP22^{174\text{-}301}$, the chimeric molecule further oligomerized in a way similar to KicGAS (Fig. 4 *D* and *E*), confirming that the KSHV α1 helix and α1–α2 linker are sufficient to induce higher order oligomerization of homologous proteins. The oligomerization enhanced both DNA binding affinity and cooperativity of the chimera molecule (Fig. 4*F*).

Modeling of Full-Length KicGAS Reveals Multiple DNA Binding Sites in KicGAS Dimer and Polymer. The KicGAS structure we determined is just 2 aa short of R97, a residue conserved in all gammaherpesviral homologs and also shown to be important for high-affinity DNA binding (15). Despite repeated efforts, none of the constructs beyond S95 at the C terminus produced crystals that diffracted to high resolution. To envision the structural basis of KicGAS binding to DNA, we extended the KSHV KicGAS dimer model to residue 104 by using the MHV-68 ORF52 structure as a template (18). In the extended dimer model, the two R97 residues are juxtaposed in the middle of two antiparallel β strands (Fig. 5*A*), constituting one prominent site for DNA binding. In KicGAS polymer, the R97 sites are present on both sides of the KicGAS chain in an alternating pattern, forming multiple binding sites for DNA, especially long DNA molecules (Fig. 5*B*). The electrostatic potential surface of the KicGAS dimer and polymer reveals additional positively charged patches that are consistent with previously identified residues (15, 16). In particular, K69, R73, and K80 extended the central R97 positive charge "peak" in both directions, forming a continuous track for DNA binding (Fig. 5*C*). At the base of α1 helix, R29, R32, and K33 cluster together, forming another prominent positively charged surface for potential DNA binding (Fig. 5*C*). DNA binding sites multiply in the polymeric assembly of KicGAS molecules, enabling stronger multivalent interactions with long DNA in particular (Fig. 5*D*).

Discussion

One function of KicGAS/ORF52 is to inhibit cGAS. This function is shared not only by KicGAS homologs in gammaherpesviruses but also by VP22 and its homologs in alphaherpesviruses (15, 16, 19, 20). Unlike poxins of poxviruses that degrade cGAS product cGAMP or other covalent modifiers of cGAS (21, 22), KicGAS-like herpesvirus tegument proteins are noncatalytic. They inhibit cGAS activity and prevent cGAMP production by blocking DNA-induced cGAS activation. We have recently shown that KicGAS oligomerization is critical for its cooperative binding to DNA and inhibition of cGAS (15). The crystal structure of $KicGAS^{9\text{-}95}$ now reveals the molecular details of how KicGAS molecules interact with each other to form oligomers, even polymers. The basic unit of KicGAS is a "Z"-shaped dimer, formed mostly by the middle long α2 helices intertwined antiparallelly while the N-terminal α1 helices stick out to form the two arms of the "Z." One arm of a "Z" dimer interacts with another arm of a different "Z" by a leucine zipper, resulting in a potentially infinite chain of "Z" dimers (Figs. 3*A* and 5 *B* and *C*). The structure also confirmed our previous observation that domain II (equivalent to α2 and α3) mediated intermolecular interaction is very stable while domain I (equivalent to α1) mediated interaction is more dynamic. In addition to several positively charged patches in $KicGAS^{9\text{-}104}$, KicGAS contains a positively charged R cluster in the C-terminal disordered region, which is very important for high-affinity DNA binding (Figs. 2*A* and 5*D*) (15). Polymerization of KicGAS conceivably increases valency for binding with negatively charged DNA, especially long DNA that elicits more robust cGAS activation. Such multivalent and cooperative interactions allow efficient phase separation of KicGAS upon binding to DNA and consequently inhibit DNA-induced phase separation and activation of cGAS. When the KicGAS α1 helix and α1–α2 linker region were grafted onto $VP22^{190\text{-}301}$, the chimeric protein assembled into higher order oligomers and bound DNA with elevated affinity, validating the role of α1 and the α1–α2 linker in mediating oligomerization and enabling multivalent interactions with DNA. Though the α1–α2 linker is more rigid than in MHV-68 ORF52, it allows movement within a small range (*SI Appendix*, Figs. S5*A* and S9). Such flexibility may enable KicGAS polymer to adopt slight curvature to better accommodate DNA binding.

Unlike the long chain polymeric KicGAS, the homolog structure of MHV-68 ORF52 is a tetramer consisting of a dimer of dimers despite both sharing the same α1–α2–α3 secondary structural arrangement (Fig. 3*D*). However, the α1–α2 linker is highly flexible in MHV-68 ORF52, so that the four α1 helices form two pairs of leucine zippers within the tetramer (Fig. 3*D*). The same linker region in KicGAS appears to be more rigid, resulting in an α1 helix pointing almost orthogonal to the α2–α3 platform. The two proline residues probably confer rigidity to this linker region, which enables KicGAS to form an infinite polymeric chain that binds preferentially to longer DNA.

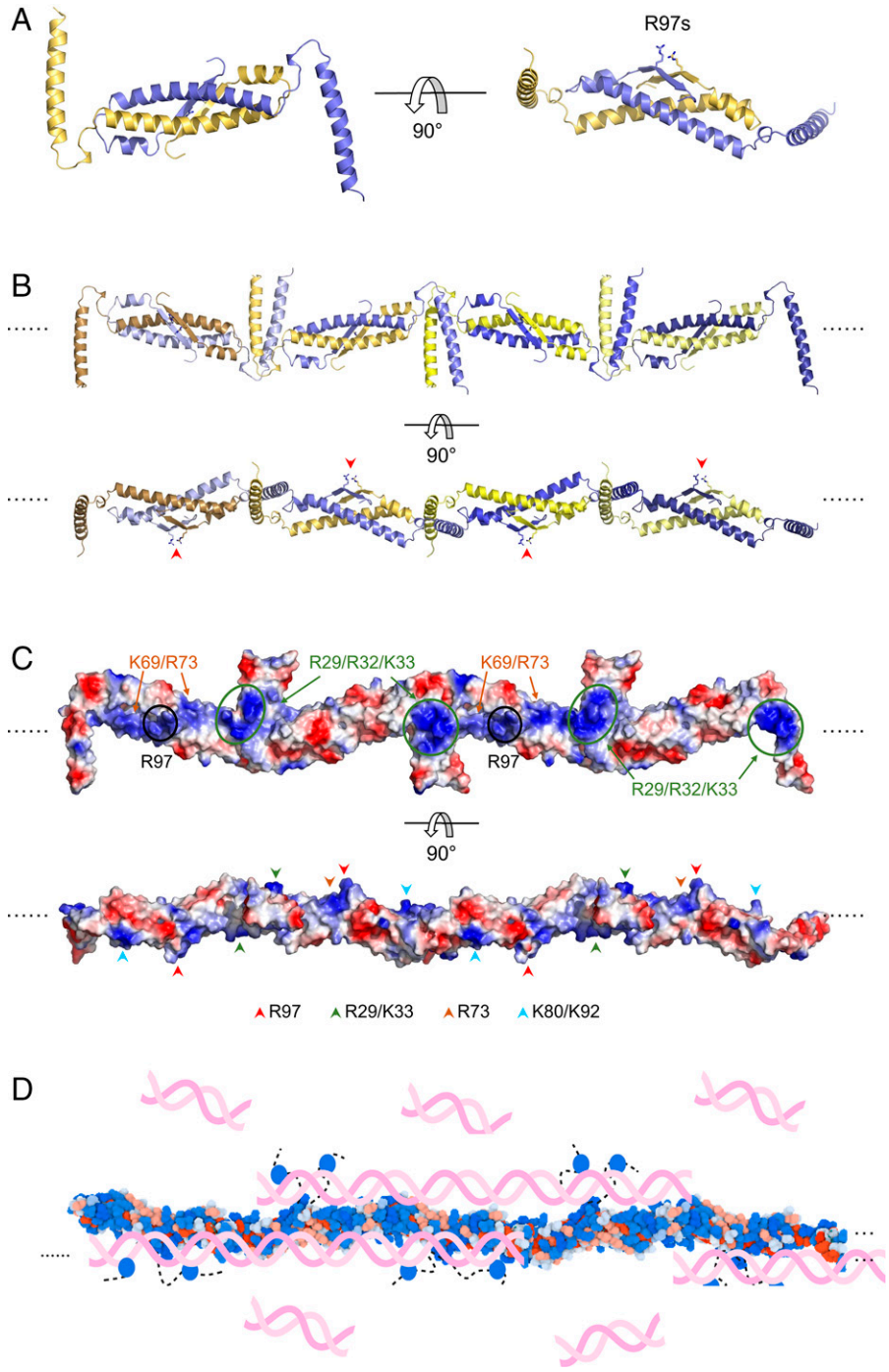

Fig. 5. Polymeric KicGAS presents multiple DNA binding sites. (*A*) Modeling of KicGAS$^{9\text{-}104}$ dimer juxtaposes the two R97 residues. (*B*) KicGAS$^{9\text{-}104}$ polymer chain in two orthogonal views. Red arrowheads point to the R97 sites. (*C*) Electrostatic surface of KicGAS$^{9\text{-}104}$ chain in two orthogonal views, highlighting multiple positively charged patches along the chain. Red, green, brown, and cyan arrowheads indicate various positively charged patches for DNA binding. (*D*) Proposed multivalent DNA binding mode of KicGAS (created with BioRender.com). Both the structured region (space-filling models) and the flexible R clusters (blue blobs connected with dashed lines) participate in DNA binding.

Interestingly, the two prolines are mostly conserved in primate gammaherpesviruses but not murine herpesviruses (Fig. 4*A* and *SI Appendix*, Fig. S8), suggesting that KicGAS homologs of primate gammaherpesviruses may exist in similar higher order oligomeric forms. Recent studies have shown that human cGAS possesses enhanced ability over mouse cGAS to preferentially detect longer DNA and favor higher order cGAS-DNA oligomerization (23). It is conceivable that KSHV has coevolved in such a way that KicGAS forms higher order oligomers to preferentially bind to longer DNA to antagonize human cGAS.

Tegument proteins usually have roles in early stages of infection to help deliver capsid into the nucleus, evade the innate immune response, and prepare the cellular environment for initial viral gene expression. They also participate in virion assembly and maturation at late stages of infection. As a major component of virion tegument, KicGAS/ORF52 is expected to perform multiple functions through interactions with various viral and cellular proteins during various phases of the infection cycle. VP22 is known to interact with several tegument and envelope glycoproteins (24, 25). It is tempting to speculate that

the polymeric KicGAS functions as a scaffold for various viral proteins to congregate and assemble. The same strategy may be used to hijack cellular processes. ORF52 of Rhesus monkey rhadinovirus (RRV), a gammaherpesvirus, has been shown to colocalize with microtubules and induce microtubule bundling and acetylation (26). A similar phenomenon was also noted for KicGAS and more prominently for VP22 (27–30). The microtubule regulating property of Rhesus monkey rhadinovirus ORF52 has been shown to rely on the N-terminal conserved leucine zipper motif. Interestingly, the counterparts of those conserved residues in KicGAS directly mediate α1 dimerization, hence KicGAS polymerization, suggesting α1 leucine zipper-mediated polymerization contributes to ORF52-induced microtubule rearrangement. Polymeric KicGAS may be an obstacle when tegument proteins are packed into budding virions. Dissociation of KicGAS into smaller oligomers or even dimers naturally resolves such a problem and allows for optimal use of space in virions. Dissociation can be induced by decreasing concentration (Fig. 1*A*) or triggered by interactions with other viral or cellular factors. The dimer form is conserved between VP22 of alphaherpesviruses and ORF52 of gammaherpesviruses, presumably representing a basic functional unit. Dynamic interaction mediated by α1 could offer a more versatile and flexible interaction platform that caters to the needs of multiple partners during various stages of the viral life cycle. It is possible that the association–dissociation equilibrium regulates microtubule organization at various stages of infection. Our structure revealed a higher order KicGAS structure noticeably different from MHV-68 ORF52. Although the functional significance of the difference awaits further clarification, the structural insights will guide future research to elucidate the various and specific roles of KicGAS in KSHV life cycle. Because changing the conserved residues results in disruption of self-oligomerization of KicGAS and similar changes in MHV68-ORF52 abolish the production of infectious progeny virions (15, 31), the conserved α1 leucine zipper–mediated intermolecular interaction could be a viable antiviral target for KSHV as well as other human and animal gammaherpesviruses.

Materials and Methods

Cloning and Mutagenesis. Full-length DNA optimized for bacterial expression of KicGAS/ORF52 protein (YP_001129405.1) was synthesized by GenScript. A truncated portion of that gene encoding residues 9–95 was cloned into a modified pRSFDuet-1 vector (Novagen) bearing an N-terminal His_6-SUMO tag. In order to express $KicGAS^{9\text{-}95}$ derivative containing a Met substitution at Leu62 (L62M), we performed site-directed mutation by using the designed primers (IDT) and the QuikChange Site-Directed Mutagenesis kit (Agilent) according to the manufacturer's instructions. Full-length KicGAS mutants, MHV-68 ORF52 (accession: AAB66445) were cloned into a modified pET28a vector with an N-terminal Avi-His_6-SUMO tag that was gifted from Dr. Pingwei Li (32). Truncated portions of the HSV-1 VP22 gene from HSV-1 (accession: ABI63510), $VP22^{174\text{-}281}$ and $VP22^{174\text{-}301}$, were cloned into the aforementioned modified pRSFDuet-1 vector. The chimeric α1-$VP22^{190\text{-}301}$ gene was synthesized from GenScript and cloned into the aforementioned modified pRSFDuet-1 vector.

Protein Expression and Purification. The SeMet KicGAS was overexpressed in *E. coli* BL21 (DE3) RIPL cells (Agilent). Cells were grown in M9 minimal media containing 50 μg/mL kanamycin, 0.4% glucose, and 2 mM $MgSO_4$. Initial growth was carried out at 37 °C until the optical density at 600 nm of the culture reached 0.6–0.8. Lysine, threonine, phenylalanine (100 mg/L each), leucine, isoleucine, valine (50 mg/L each), and L(+)selenomethionine (SeMet) (50 mg/L) were added to the culture. The incubation temperature was then decreased to 20 °C, and protein expression was induced by adding isopropyl-D-thiogalactopyranoside to a final concentration of 0.4 mM. After overnight incubation, the cells were harvested by centrifugation. Cells were lysed by sonication in Lysis Buffer (20 mM phosphate buffer [pH 7.4], 300 mM NaCl, 10% glycerol, 30 mM imidazole, and 1 mM DTT). Clarified lysate was bound to Ni-NTA agarose (Qiagen), and resin was washed extensively with Lysis Buffer supplemented with 1 M NaCl. The bound protein was eluted with Lysis Buffer supplemented with 300 mM imidazole. The eluted SeMet-derivatized protein was dialyzed in Buffer A (10 mM Tris HCl, pH 7.5, 150 mM NaCl). The purified proteins were cleaved with SUMO protease Ulp1 (1:1,000 wt/wt) at 4 °C overnight. The His_6-SUMO tag was removed with a Ni-NTA column, and the target proteins in the flow-through were further purified by a heparin column with a linear gradient of 150–1,000 mM NaCl in 20 mM Tris·HCl, pH 7.5. Protein from peak fractions was pooled and further purified by size exclusion chromatography on a Superdex 200 HiLoad 16/600 column pre-equilibrated with Buffer A. Purified tag-free SeMet $KicGAS^{9\text{-}95}$ (L62M) protein was then concentrated to 12 mg/mL through Amicon Ultra Centrifugal Filters, flash frozen in liquid nitrogen, aliquoted, and stored at –80 °C. Full-length KicGAS and mutants, MHV-68 ORF52, VP22 proteins, and the chimeric VP22 protein were purified similarly, except that the NaCl concentration was 300 mM in the size exclusion chromatography running buffer.

Crystallization. Crystals were grown at 16 °C by hanging drop vapor diffusion method. One microliter of $KicGAS^{9\text{-}95}$ (L62M) solution (12 mg/mL in Buffer A) was mixed with 1 μL of reservoir solution consisting of 9% (vol/vol) polyethylene glycol 3350 (PEG 3350), 100 mM Na-citrate pH 4.5, and 0.2 μL of the detergent additive n-Octyl-N,*N*-dimethyl-3-ammonio-1-propanesulfonate (Hampton Research). The crystals were cryoprotected with perfluoropolyether cryo oil (Hampton Research) and flash frozen in liquid nitrogen for data collection.

Data Collection and Structure Determination. Diffraction data were collected at Automated Macromolecular Crystallography beamline 17-ID-1 of the National Synchrotron Light Source II. The data were indexed, integrated, and scaled with the HKL2000 package (33). The structure was determined by molecular replacement coupled with single-wavelength anomalous diffraction using Phenix (34). The search model was a modified version of MHV-68 ORF52 protein (PDB ID 2OA5) (18). SeMet sites were then determined from the top solution from the MR search. Iterative model building and refinements were carried out in Coot (35) and Phenix (34).

Analytical Ultracentrifugation. Analytical ultracentrifugation experiments were carried out with a Beckman Coulter Optima XL-I ultracentrifuge with samples in a buffer containing 20 mM Tris·HCl pH 7.5 and 150 mM NaCl. The sample was loaded into two-sector Epon centerpieces in an An60 Ti rotor and run at 5 °C. Measurement was completed in intensity mode. The concentration of the protein used in this study was 10 μM. The experiment was run at 55,000 rpm (243,500 × *g*). Partial specific volume was based on the weight averages of the partial specific volumes of the KicGAS protein (0.736 mL/g). Solution density and viscosity were calculated with the buffer data from the UltraScan3 database. All SV-AUC data were analyzed in UltraScan3 software, version 4.0 and release 6029 (36). Data editing and refinement were performed according to the protocol as described (36). Briefly, the sedimentation coefficient range is estimated from an enhanced van Holde–Weischet analysis. Two-dimensional spectrum analysis (2DSA) was performed to subtract time-invariant noise, and the meniscus was fit with 10 points in a 0.03-cm range. Arrays were fit with an S range of 1–6 S and an f/f_0 range of 1–4 with 64 grid points for each. 2DSA was then repeated at the determined meniscus to fit radially invariant and time-invariant noise together through 10 iterations. Final 2DSA was performed with 50 Monte Carlo iterations. van Holde–Weischet analysis was completed by using these noise subtraction profiles to determine S.

cGAS Inhibition Assay. cGAS activity assay was performed in the presence of purified KicGAS, its mutants, and truncated constructs of KicGAS. A fluorescent analog of adenosine triphosphate (2-aminopurine riboside-5′-O-triphosphate; Jena Biosciences) was used (15, 37). Briefly, 400 nM ISD45 (interferon stimulatory DNA, a 45-bp non-CpG oligomer from the *Listeria monocytogenes* genome) (38) was premixed with various concentrations of KicGAS proteins, after which 400 nM cGAS in 40 mM Tris pH 7.5, 100 mM NaCl, and 200 μM Zn^{2+} was added. The reaction was started by adding 5 mM $MgCl_2$ with 500 μM GTP and 50 μM 2-aminopurine riboside-5′-O-triphosphate. Fluorescence decrease was measured in 384-well black nonbinding polymer surface plates (Greiner

Bio-One/Corning) on a SpectraMax iD5 or a Tecan SPARK plate reader (λex = 307 nm, λem = 370 nm). The background fluorescence was subtracted from the initial fluorescence curve, and the resulting curves were inverted for better visualization (37).

DNA Binding Assay. DNA binding was examined by measuring fluorescence polarization values in a multimode microplate reader (Biotek Instruments/Tecan SPARK) with 384-well black nonbinding polymer surface plates (Greiner Bio-One/Corning). Increasing concentrations of proteins were added to a fixed concentration of FAM-dsISD45. Fluorescence polarization values were plotted as a function of protein concentration and fitted to the Hill equation in Origin version 8.5.

Turbidity Assay. Turbidity assays were performed by incubating 10 μM KicGAS wild-type or mutant proteins with 10 μM ISD100 in a Nunc 384-well transparent microplate for 30 min in the buffers containing various NaCl concentrations (100–400 mM). Turbidity was detected by measuring the absorbance at 340 nm with a SpectraMax iD5 plate reader. The absorbance values were plotted against NaCl concentrations in Origin version 8.5.

Negative-Stain Electron Microscopy. Freshly purified KicGAS$^{9\text{-}95}$ solutions (in 20 mM Tris pH 7.5, 200 mM NaCl) were applied to glow-discharged, carbon-coated electron microscopy grids for 1 min, blotted off with filter paper, flash washed with ultrapure water twice, then stained with 2% uranyl acetate for 30 s. Excess stain was aspirated, and the grid was allowed to dry at ambient temperature. Images were collected on a Hitachi HT7800 120-kV transmission electron microscope at the Biological Science Imaging Resource facility at Florida State University.

Data, Materials, and Software Availability. The atomic coordinates, structure factors, and X-ray crystal diffraction data have been deposited in the Protein Data Bank at https://www.wwpdb.org/pdb?id=pdb_00007tdq, (PDB ID code 7TDQ) (39).

ACKNOWLEDGMENTS. This work was supported by National Institutes of Health/National Institute of Allergy and Infectious Diseases grants R00AI108793 and R01AI146330 and National Institutes of Health/National Institute of General Medical Science grant R01GM138685 to Qian Yin, and National Institutes of Health/National Institute of Dental & Craniofacial Research grant R01DE026101 to Fanxiu Zhu. We thank Dr. Borries Demeler for guidance on SV-AUC data interpretation. We thank members of the Zhu and Yin laboratories for critical readings of the manuscript and for helpful discussions. We also thank all the staff scientists at the Biological Science Imaging Resource at FSU and Automated Macromolecular Crystallography and Frontier Macromolecular Crystallography beamlines at National Synchrotron Light Source II at Brookhaven National Laboratory for assistance in data collection. We thank the Advanced Photon Source summer school for providing a free virtual workshop to Debipreeta Bhowmik.

1. P. J. Kranzusch, cGAS and CD-NTase enzymes: Structure, mechanism, and evolution. *Curr. Opin. Struct. Biol.* **59**, 178–187 (2019).
2. L. Sun, J. Wu, F. Du, X. Chen, Z. J. Chen, Cyclic GMP-AMP synthase is a cytosolic DNA sensor that activates the type I interferon pathway. *Science* **339**, 786–791 (2013).
3. K.-P. Hopfner, V. Hornung, Molecular mechanisms and cellular functions of cGAS-STING signalling. *Nat. Rev. Mol. Cell Biol.* **21**, 501–521 (2020).
4. J. Wu *et al.*, Cyclic GMP-AMP is an endogenous second messenger in innate immune signaling by cytosolic DNA. *Science* **339**, 826–830 (2013).
5. G. T. Melroe, N. A. DeLuca, D. M. Knipe, Herpes simplex virus 1 has multiple mechanisms for blocking virus-induced interferon production. *J. Virol.* **78**, 8411–8420 (2004).
6. T. Tabtieng, R. C. Lent, A. M. Sanchez, M. M. Gaglia, Analysis of caspase-mediated regulation of the cGAS/STING pathway in Kaposi's sarcoma-associated herpesvirus lytic infection reveals a dramatic cellular heterogeneity in type I interferon responses. bioRxiv [Preprint] (2021). https://doi.org/10.1101/2021.05.03.442439. Accessed 29 December 2021.
7. A. L. Verzosa *et al.*, Herpes simplex virus 1 infection of neuronal and non-neuronal cells elicits specific innate immune responses and immune evasion mechanisms. *Front. Immunol.* **12**, 644664 (2021).
8. D. Bhowmik, F. Zhu, Evasion of intracellular DNA sensing by human herpesviruses. *Front. Cell. Infect. Microbiol.* **11**, 647992 (2021).
9. J. B. Eaglesham, P. J. Kranzusch, Conserved strategies for pathogen evasion of cGAS-STING immunity. *Curr. Opin. Immunol.* **66**, 27–34 (2020).
10. J. J. Wu *et al.*, Inhibition of cGAS DNA sensing by a herpesvirus virion protein. *Cell Host Microbe* **18**, 333–344 (2015).
11. E. Cesarman *et al.*, Kaposi sarcoma. *Nat. Rev. Dis. Primers* **5**, 9 (2019).
12. Y. Chang *et al.*, Identification of herpesvirus-like DNA sequences in AIDS-associated Kaposi's sarcoma. *Science* **266**, 1865–1869 (1994).
13. J. Soulier *et al.*, Kaposi's sarcoma-associated herpesvirus-like DNA sequences in multicentric Castleman's disease. *Blood* **86**, 1276–1280 (1995).
14. K. Hew, S.-L. Dahlroth, L. X. Pan, T. Cornvik, P. Nordlund, VP22 core domain from Herpes simplex virus 1 reveals a surprising structural conservation in both the Alpha- and Gammaherpesvirinae subfamilies. *J. Gen. Virol.* **96**, 1436–1445 (2015).
15. D. Bhowmik *et al.*, Cooperative DNA binding mediated by KicGAS/ORF52 oligomerization allows inhibition of DNA-induced phase separation and activation of cGAS. *Nucleic Acids Res.* **49**, 9389–9403 (2021).
16. G. Xu *et al.*, Viral tegument proteins restrict cGAS-DNA phase separation to mediate immune evasion. *Mol. Cell* **81**, 2823–2837.e9 (2021).
17. B. Demeler, Methods for the design and analysis of sedimentation velocity and sedimentation equilibrium experiments with proteins. *Curr. Protoc. Protein Sci.* **Chapter 7**, Unit 7.13 (2010).
18. J. Benach *et al.*, Structural and functional studies of the abundant tegument protein ORF52 from murine gammaherpesvirus 68. *J. Biol. Chem.* **282**, 31534–31541 (2007).
19. J. Huang *et al.*, Herpes simplex virus 1 tegument protein VP22 abrogates cGAS/STING-mediated antiviral innate immunity. *J. Virol.* **92**, JVI.00841-18 (2018).
20. J. Hertzog *et al.*, Varicella-zoster virus ORF9 is an antagonist of the DNA sensor cGAS. bioRxiv [Preprint] (2021). https://doi.org/10.1101/2020.02.11.943415.
21. J. B. Eaglesham, Y. Pan, T. S. Kupper, P. J. Kranzusch, Viral and metazoan poxins are cGAMP-specific nucleases that restrict cGAS-STING signalling. *Nature* **566**, 259–263 (2019).
22. J. Zhang *et al.*, Species-specific deamidation of cGAS by herpes simplex virus UL37 protein facilitates viral replication. *Cell Host Microbe* **24**, 234–248.e5 (2018).
23. W. Zhou *et al.*, Structure of the human cGAS-DNA complex reveals enhanced control of immune surveillance. *Cell* **174**, 300–311.e11 (2018).
24. K. Maringer, J. Stylianou, G. Elliott, A network of protein interactions around the herpes simplex virus tegument protein VP22. *J. Virol.* **86**, 12971–12982 (2012).
25. L. Wu *et al.*, Alphaherpesvirus major tegument protein VP22: Its precise function in the viral life cycle. *Front. Microbiol.* **11**, 1908 (2020).
26. M. S. Loftus, N. Verville, D. H. Kedes, A conserved leucine zipper motif in gammaherpesvirus ORF52 is critical for distinct microtubule rearrangements. *J. Virol.* **91**, e00304–e00317 (2017).
27. G. Elliott, P. O'Hare, Herpes simplex virus type 1 tegument protein VP22 induces the stabilization and hyperacetylation of microtubules. *J. Virol.* **72**, 6448–6455 (1998).
28. A. Kotsakis, L. E. Pomeranz, A. Blouin, J. A. Blaho, Microtubule reorganization during herpes simplex virus type 1 infection facilitates the nuclear localization of VP22, a major virion tegument protein. *J. Virol.* **75**, 8697–8711 (2001).
29. W. Li *et al.*, Kaposi's Sarcoma-associated herpesvirus inhibitor of cGAS (KicGAS), encoded by ORF52, is an abundant tegument protein and is required for production of infectious progeny viruses. *J. Virol.* **90**, 5329–5342 (2016).
30. A. Martin, P. O'Hare, J. McLauchlan, G. Elliott, Herpes simplex virus tegument protein VP22 contains overlapping domains for cytoplasmic localization, microtubule interaction, and chromatin binding. *J. Virol.* **76**, 4961–4970 (2002).
31. L. Wang *et al.*, Distinct domains in ORF52 tegument protein mediate essential functions in murine gammaherpesvirus 68 virion tegumentation and secondary envelopment. *J. Virol.* **86**, 1348–1357 (2012).
32. B. Zhao *et al.*, Structural basis for concerted recruitment and activation of IRF-3 by innate immune adaptor proteins. *Proc. Natl. Acad. Sci. U.S.A.* **113**, E3403–E3412 (2016).
33. Z. Otwinowski, W. Minor, Processing of X-ray diffraction data collected in oscillation mode. *Methods Enzymol.* **276**, 307–326 (1997).
34. D. Liebschner *et al.*, Macromolecular structure determination using X-rays, neutrons and electrons: Recent developments in Phenix. *Acta Crystallogr. D Struct. Biol.* **75**, 861–877 (2019).
35. P. Emsley, B. Lohkamp, W. G. Scott, K. Cowtan, Features and development of Coot. *Acta Crystallogr. D Biol. Crystallogr.* **66**, 486–501 (2010).
36. B. Demeler, G. E. Gorbet, "Analytical ultracentrifugation data analysis with ultrascan-III" in *Analytical Ultracentrifugation: Instrumentation, Software, and Applications*, S. Uchiyama, F. Arisaka, W. F. Stafford, T. Laue, Eds. (Springer, Japan, Tokyo, 2016), pp. 119–143. 10.1007/978-4-431-55985-6_8.
37. L. Andreeva *et al.*, cGAS senses long and HMGB/TFAM-bound U-turn DNA by forming protein-DNA ladders. *Nature* **549**, 394–398 (2017).
38. D. B. Stetson, R. Medzhitov, Recognition of cytosolic DNA activates an IRF3-dependent innate immune response. *Immunity* **24**, 93–103 (2006).
39. Q. Yin *et al.*, "Crystal Structure of KSHV KicGAS/ORF52." Protein Data Bank. https://www.wwpdb.org/pdb?id=pdb_00007tdq. Deposited 3 January 2022.